

Multiple rebrightenings in the optical afterglow of GRB 210731A: evidence for an asymmetric jet

JIN-DA LI,^{1,2} HE GAO,^{1,2} SHUNKE AI,^{3,4} AND WEI-HUA LEI⁵

¹*Institute for Frontier in Astronomy and Astrophysics, Beijing Normal University, Beijing 102206, China*

²*School of Physics and Astronomy, Beijing Normal University, Beijing 100875, China*

³*Department of Astronomy, School of Physics and Technology, Wuhan University, Wuhan 430072, China*

⁴*Niels Bohr International Academy and DARK, Niels Bohr Institute, University of Copenhagen, Blegdamsvej 17, 2100, Copenhagen, Denmark*

⁵*Department of Astronomy, School of Physics, Huazhong University of Science and Technology, Wuhan, Hubei 430074, China*

ABSTRACT

The broadband afterglow of Gamma-ray bursts (GRBs) is usually believed to originate from the synchrotron radiation of electrons accelerated by the external shock of relativistic jets. Therefore, the jet structure should have a significant impact on the GRB afterglow features. The latest observations indicate that the GRB jets may possess intricate structures, such as Gaussian structure, power-law structure, or jet-cocoon structure. Most recently, an abnormal afterglow of GRB 210731A has raised extensive attention, whose optical afterglow exhibits multiple rebrightening phenomena within 4 hours, posing a serious challenge to the standard afterglow model. Here we intend to interpret the characteristics of GRB 210731A afterglows within the framework of non-axisymmetric structured jets, where multiple distinct peaks in the afterglow light curve are caused by the uneven distribution of energy and velocity within the jet in the azimuth angle direction. Through Monte Carlo Markov Chain fitting, we show that a three-component asymmetric structured jet can well explain the multi-band afterglow data. The energy difference among the three components is about 1.5 orders of magnitude, with higher-energy components exhibiting slower speeds. The radiation contribution of each component has sequentially dominated the light curve of the afterglow, resulting in multiple peaks, with the highest peak occurring at the latest time. We suggest that in the future, polarization observations should be conducted on afterglows with multiple brightening signatures, which will help to effectively distinguish the structured jet model from other alternative models, such as energy injection, and ultimately help to determine the true configuration of jets.

Keywords: Gamma-ray bursts (GRBs)

1. INTRODUCTION

Multiwavelength observations of GRB afterglows were predicted before their first discoveries (Mészáros & Rees 1997; Costa et al. 1997; Frail et al. 1997; van Paradijs et al. 1997), based on a generic external forward shock model. This model, which is independent of the physical nature of the progenitor and central engine, assumes that a relativistic jet is launched and subsequently decelerated by a circumburst medium through a pair of external shocks - forward and reverse. It is likely that the reverse shock is short-lived, while the forward shock continues to plow into the medium as the jet is decelerated. The synchrotron radiation of electrons accelerated from the external forward shock powers the broadband electromagnetic radiation with a decreasing amplitude, forming the broadband afterglow of GRBs (Gao et al. 2013, for a review).

With a large sample of GRBs with both X-ray and optical afterglow data, Wang et al. (2015) perform a systematic study to conclude that the simplest external forward shock models can account for the multiwavelength afterglow data of at least half of the GRBs. The remaining GRB afterglows may exhibit some features that deviate from the

predictions of the simplest model, but it is these features that allow us to study the central engine and jet structure of GRBs using the afterglow. For example, through the appearance of flares in the afterglow, we can recognize the reactivation of the central engine (Zhang et al. 2006), and through the slow decay component, we can understand the continuous energy injection of the central engine and determine that some GRBs may have a magnetic star as their central engine (Dai & Lu 1998; Zhang et al. 2006). When more advanced modeling (e.g., long-lasting reverse shock, structured jets, arbitrary circumburst medium density profile) is invoked, Wang et al. (2015) found that up to $> 90\%$ of the afterglows could be interpreted within the framework of the external shock models.

Most recently, an abnormal afterglow of GRB 210731A has raised extensive attention (de Wet et al. 2023). GRB 210731A was a long-duration ($T_{90} = 22.5$ s) gamma-ray burst discovered by the Burst Alert Telescope (BAT) aboard the Neil Gehrels *Swift* Observatory (Gehrels et al. 2004). The multi-band observation of the afterglow used the wide-field, robotic MeerLICHT optical telescope in Sutherland showed a light curve with three similar peaks in brightness within the first four hours (de Wet et al. 2023). The first optical peak can be explained as the onset of afterglow, while the other two peaks are taken as subsequent re-brightenings. This multiple rebrightening phenomenon cannot be explained by a simple external shock model. One possible explanation is multiple energy injection (e.g., Mangano et al. 2007; Greiner et al. 2009; Swenson et al. 2013). However, if one uses this model to interpret the data of GRB 210731A, it would require that the final energy injection is at least 1000 times the initial energy (de Wet et al. 2023), which means that the central engine’s reactivation strength is 1000 times the initial activity strength, and there is no corresponding signature of reactivation in gamma-ray or X-ray emissions, which is puzzling.

In addition to the energy injection, structured jet scenarios can also cause late-time afterglow deviations from the standard model. For example, Gaussian structured jets or power-law structured jets would cause the afterglow decay slope to be shallower (Beniamini et al. 2020; Gottlieb et al. 2021), while two-component structured jets would lead to a late-time rebrightening feature (Huang et al. 2004; Peng et al. 2005). However, these axially symmetric structured jets would have difficulties explaining the multiple similar rebrightening signatures in GRB 210731A. Most recently, Li et al. (2023) discussed the potential characteristics of GRB afterglows within the framework of non-axisymmetric structured jets, whose results suggested that the uneven distribution of energy and velocity within the jet in the azimuth angle direction will cause multiple distinct peaks in the late afterglow light curve.

In this work, we intend to fit the multi-band afterglow data of GRB 210731A using Monte Carlo Markov Chain (MCMC) method under the model of asymmetric structured jet, in order to determine whether GRB 210731A was a good candidate produced by an asymmetric structured jet.

2. GRB 210731A DATA

GRB 210731A was observed by the *Swift* Burst Alert Telescope (BAT; Barthelmy et al. 2005) at 22:21:08 UT on July 31, 2021. We set the time when *Swift* BAT being triggered as $T = 0$. It has a single pulse structure at the light curve of 15–350 keV, and the duration T_{90} is 22.5 ± 2.8 s (Stamatikos et al. 2021). ~ 200 seconds after the BAT trigger, the *Swift* X-Ray Telescope (XRT, Burrows et al. 2005) commenced its observation of the GRB 210731A’s field and detected a prominent new X-ray source that correlated with the BAT’s reported position, as documented by Troja et al. (2021). And a rapid decrease in X-ray radiation flow was observed in the following 62 seconds. The observations from 10ks to 20ks after trigger show a platform. Then, the radiation flux has continued to decrease.

210 seconds after the trigger event, the *Swift* UltraViolet and Optical Telescope (UVOT, Roming et al. 2005) began observing the field and capturing a single exposure of 61.7 seconds using a white filter. Starting approximately 3.27 hours after trigger, various filters were used intermittently for the following five days to continue observation (Troja et al. 2021; Kuin et al. 2021).

The wide-field, robotic MeerLICHT optical telescope in Sutherland (Bloemen et al. 2016) was triggered by *Swift*. 286 seconds after the *Swift* trigger, it began observing the BAT error circle. In its initial 60-second q-band exposure, the optical afterglow of GRB 210731A was detected. The observation lasted for approximately 4.29 hours after trigger, and continue to track the decline of afterglow in the following days. There are three peaks of comparable brightness appeared in MeerLicht’s first four hours of multi-band observation (de Wet et al. 2023). The abnormal optical afterglow prompted a series of multi-wavelength follow-up observations, covering a spectrum ranging from X-ray to radio frequencies:

- Within 4.2 hours after GRB trigger, the Gamma-Ray Burst Optical Near-Infrared Detector (GROND, Greiner et al. 2008) which installed on the 2.2 m MPG telescope at the La Silla Observatory of the European Southern Observatory (ESO) in Chile observed the afterglow of GRB 210731A in the g' , r' , i' , z' , J, H and K bands (Nicsusa

Guelbenzu et al. 2021a). The subsequent observations were conducted on 1.225 days, 2.214 days, and 5.253 days (Nieves Guelbenzu et al. 2021b).

- At 9.04 hours after trigger, the 76cm Kazmann Automatic Imaging Telescope (KAIT, Filippenko et al. 2001) at the Lick Observatory observed afterglow in the *clear* band (Zheng et al. 2021).
- After the *Swift* BAT was triggered for 1.18 days, the acquisition camera of the X-shooter spectrograph which installed on the ESO Very Large Telescope (VLT) UT3 (Meripal) obtained images in the *r*, *g* and *z* bands. And on 1.19 days after trigger, the X-Shooter on the Very Large Telescope obtained the afterglow redshift of $z = 1.2525$ (Kann et al. 2021).
- In C and X bands, *Karl G. Jansky* Very Large Array (JVLA Perley et al. 2011) conducted four observations from 18.2 to 118 days after trigger. In L-band, de Wet et al. (2023) used the MeerKAT radio telescope to observe it on 10.8, 34.1, and 59.7 days after trigger, but no afterglow was observed. They set three times the root mean square noise as the upper limit of the L-band afterglow flux.

In this work, we used the multiband data collected in (de Wet et al. 2023), which is shown in Figure 3.

3. MODEL DESCRIPTION

Li et al. (2023) have established theoretical descriptions of asymmetric jet structures. In order to discuss the influence of asymmetric structures, they simply assumed that the jet is uniform in the direction of the polar angle θ . And a jet with an asymmetric structure can be divided into N elements based on different physical parameters at different positions. Each element could be taken as a uniform "patch" and Each "patch" can be considered independent. However, in more realistic situations, asymmetric structures are likely to be nonuniform in the direction of the polar angle θ . Gill & Granot (2023) described the asymmetric structure of the jets during the GRBs' prompt emission stage with individual blobs or mini-jets (MJs) with multiple distinct properties or patches, which can be generated by a kind of hydrodynamic or hydromagnetic disturbance. It can be expected that this asymmetric structure may remain in the jet after the prompt emission stage and affect afterglow emission. Figure 1 depicts a schematic diagram of an asymmetric jet's cross-section with three components or MJs. The Lorentz factors and equivalent isotropic kinetic energies corresponding to the three components are $\gamma_{0,1}$, $E_{k,iso,1}$, $\gamma_{0,2}$, $E_{k,iso,2}$ and $\gamma_{0,3}$, $E_{k,iso,3}$. If we take the assumed jet axis as the origin (0,0) and define the angle between a point on the jet and the axis as the polar angle θ , and the circumferential direction around the jet axis as the azimuth angle φ , we can establish a polar coordinate on the cross-section of the jet (see Figure 1). The axes of the three components are represented in polar coordinate as the corresponding polar angles and azimuth angles: (θ_1, φ_1) , (θ_2, φ_2) , (θ_3, φ_3) . And the half-opening angle of each component can be represented by $\theta_{r,1}$, $\theta_{r,2}$ and $\theta_{r,3}$. Assuming there is no overlap between three components, this structure can be mathematically represented as:

$$\gamma_0 = \begin{cases} \gamma_{0,1} & \theta < \theta_1 + \theta_{r,1} \cos(\varphi - \varphi_1), \\ \gamma_{0,2} & \theta < \theta_2 + \theta_{r,2} \cos(\varphi - \varphi_2), \\ \gamma_{0,3} & \theta < \theta_3 + \theta_{r,3} \cos(\varphi - \varphi_3), \end{cases} \quad (1)$$

$$E_{k,iso} = \begin{cases} E_{k,iso,1} & \theta < \theta_1 + \theta_{r,1} \cos(\varphi - \varphi_1), \\ E_{k,iso,2} & \theta < \theta_2 + \theta_{r,2} \cos(\varphi - \varphi_2), \\ E_{k,iso,3} & \theta < \theta_3 + \theta_{r,3} \cos(\varphi - \varphi_3). \end{cases} \quad (2)$$

For the i -th component, the dynamic evolution is calculated based on Huang et al. (2000). The evolution of the jet's radius R over time T in the frame of an on-axis observer can read as:

$$\frac{dR}{dT} = \beta c \gamma (\gamma + \sqrt{\gamma^2 - 1}), \quad (3)$$

where γ is the Lorentz factor of the jet's bulk motion, while β is the dimensionless velocity corresponding to it. The mass of the interstellar medium swept by the component m with a radius of R can be described as:

$$\frac{dm}{dR} = R^2 (1 - \cos \theta_{r,i}) n m_p, \quad (4)$$

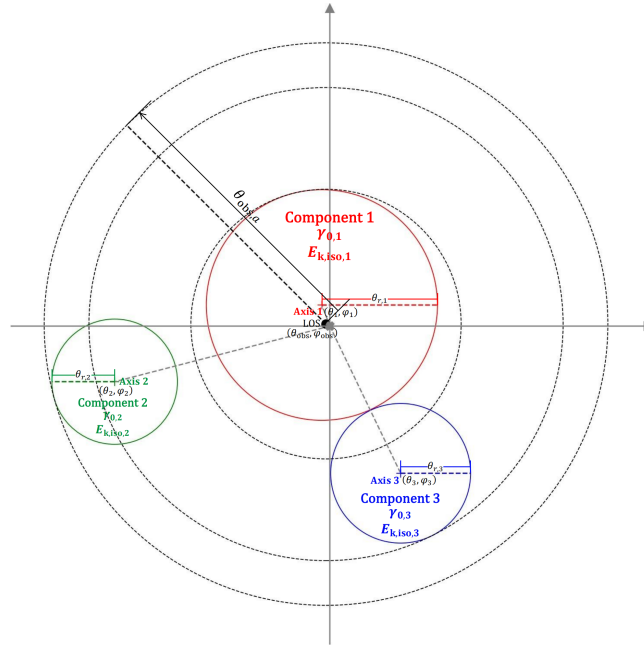


Figure 1. The schematic diagram represents the cross-section of an asymmetric jet. The jet consists of three components (the solid line circles with different colors), which have different initial Lorentz factor γ_0 and equivalent isotropic kinetic energy $E_{k,iso}$. We assume that different components don't have overlapping regions on the cross-section. Taking the assumed jet axis as the coordinate origin $(0, 0)$, the projection of LOS on the cross-section and the axis of each component can be expressed in polar coordinates as $(\theta_{obs}, \varphi_{obs})$, (θ_1, φ_1) , (θ_2, φ_2) , (θ_3, φ_3) , respectively. And the half-opening angle of each component is $\theta_{r,1}$, $\theta_{r,2}$ and $\theta_{r,3}$. The point sources on the loop around the LOS on the jet (the dash line circles) have equal values of $\theta_{obs,a}$.

where m_p is the mass of proton. The particle number density of the interstellar medium, n , can be described as AR^{-k} , where k is the wind profile variable. For the uniform interstellar medium, $k = 0$. And for the stellar wind environment, $k = 2$. A is a constant. $\theta_{r,i}$ represents the half-opening angle of the i -th component. Here the lateral spread of the jet is ignored, therefore $\theta_{r,i}$ is a constant. Considering the radiation cooling effect, the evolution of jet's bulk motion Lorentz factor γ with respect to m can be written as (Huang et al. 1999a,b):

$$\frac{d\gamma}{dm} = -\frac{\gamma^2 - 1}{M_{ej} + \epsilon m + 2(1 - \epsilon)\gamma m}, \quad (5)$$

where $M_{ej} = E_0/(\gamma_0 c^2)$ is the ejecta mass, and E_0 is the initial kinetic energy of a component. The ϵ is radiative efficiency, which is defined as the proportion of the internal energy generated by the shock in jet's comoving frame that would be radiated, which can be described as (Dai & Lu 1999):

$$\epsilon = \epsilon_e \frac{t'_{syn}{}^{-1}}{t'_{syn}{}^{-1} + t'_{ex}{}^{-1}}, \quad (6)$$

where $t'_{syn} = 6\pi m_e c / (\sigma_T B'^2 \gamma_{e,min})$ is the synchrotron cooling timescale, and $t'_{ex} = R/(\gamma c)$ is the expansion timescale in the jet's comoving frame. The σ_T stands for the cross section for Thompson scattering, and the m_e stands for the mass of electron. Assuming a fraction ϵ_B as the proportion of the total internal energy generated by shock goes into the random magnetic field, thus, the magnetic energy density in the jet's comoving frame can be estimated as

$$\frac{B'^2}{8\pi} = \epsilon_B^2 \frac{\hat{\gamma}\gamma + 1}{\hat{\gamma} - 1} (\gamma - 1) n m_p c^2, \quad (7)$$

where $\hat{\gamma} = (4\gamma + 1)/(3\gamma)$ is the adiabatic index (Dai & Lu 1999). Assuming a fraction ϵ_e as the proportion of the total internal energy generated by shock goes into the electrons. And we assume that the accelerated electrons in the interstellar medium have a power-law distribution with an index of p ($dN_e/d\gamma_e \propto \gamma_e^{-p}$). Thus, in the jet's comoving

frame, the minimum Lorentz factor for the random motion of electrons can be derived as (Huang et al. 2000)

$$\gamma_{e,\min} = \epsilon_e (\gamma - 1) \frac{m_p (p - 2)}{m_e (p - 1)} + 1. \quad (8)$$

For synchrotron radiation, the characteristic frequency and the observed radiation power of an electron with Lorentz factor γ_e are given by (Sari et al. 1998)

$$\nu(\gamma_e) = \gamma \gamma_e^2 \frac{q_e B}{2\pi m_e c}. \quad (9)$$

$$P(\gamma_e) = \frac{4}{3} \sigma_T d \gamma^2 \gamma_e^2 \frac{B^2}{8\pi}, \quad (10)$$

where q_e is the charge of an electron. The characteristic frequency $\nu(\gamma_e)$ corresponds to the peak power of the spectrum, which can be estimated as

$$P_{\nu,\max} \approx \frac{P(\gamma_e)}{\nu(\gamma_e)} = \frac{m_e c^2 \sigma_T}{3q_e} \gamma B. \quad (11)$$

Sari et al. (1998) defined a characteristic Lorentz factor γ_c as

$$\gamma_c = \frac{6\pi m_e c}{\sigma_T B^2 T} = \frac{3m_e}{16\epsilon_B \sigma_T m_p c T \gamma^3 n}. \quad (12)$$

The electrons with Lorentz factors exceeding γ_c should have significantly cooled.

The two characteristic emission frequencies ν_m and ν_c in the synchrotron spectrum are defined by the electron Lorentz factors $\gamma_{e,\min}$ and γ_c . In an $n = Ar^{-k}$ environment, for the slow cooling regime ($\nu_c > \nu_m$), the self absorption frequency ν_a is

$$\nu_a = \begin{cases} \left[\frac{c_1 q_e n R}{(3-k) B \gamma_c^5} \right]^{3/5} \nu_m & \nu_a < \nu_m, \\ \left[\frac{c_2 q_e n R}{(3-k) B \gamma_c^5} \right]^{2/(p+4)} \nu_m & \nu_m < \nu_a < \nu_c, \\ \left[\frac{c_2 q_e n R}{(3-k) B \gamma_c^5} \right]^{2/(p+5)} \left(\frac{\nu_c}{\nu_m} \right)^{1/(p+5)} \nu_m & \nu_c < \nu_a. \end{cases} \quad (13)$$

c_1 and c_2 are coefficients dependent on p (Wu et al. 2003). Assuming a point source is on the LOS, the observed flux density F_ν is divided into the following three situations

(1) $\nu_a < \nu_m < \nu_c$:

$$F_\nu = F_{\nu,\max} \begin{cases} \left(\frac{\nu}{\nu_a} \right)^2 \left(\frac{\nu_a}{\nu_m} \right)^{1/3} & \nu < \nu_a, \\ \left(\frac{\nu}{\nu_m} \right)^{1/3} & \nu_a < \nu < \nu_m, \\ \left(\frac{\nu}{\nu_m} \right)^{-(p-1)/2} F_{\nu,\max} & \nu_m < \nu < \nu_c, \\ \left(\frac{\nu}{\nu_m} \right)^{-(p-1)/2} \left(\frac{\nu}{\nu_c} \right)^{-p/2} & \nu_c < \nu. \end{cases} \quad (14)$$

(2) $\nu_m < \nu_a < \nu_c$:

$$F_\nu = F_{\nu,\max} \begin{cases} \left(\frac{\nu}{\nu_m} \right)^2 \left(\frac{\nu_m}{\nu_a} \right)^{(p+4)/2} F_{\nu,\max} & \nu < \nu_m, \\ \left(\frac{\nu}{\nu_a} \right)^{5/2} \left(\frac{\nu_a}{\nu_m} \right)^{-(p-1)/2} F_{\nu,\max} & \nu_m < \nu < \nu_a, \\ \left(\frac{\nu}{\nu_m} \right)^{-(p-1)/2} F_{\nu,\max} & \nu_a < \nu < \nu_c, \\ \left(\frac{\nu}{\nu_m} \right)^{-(p-1)/2} \left(\frac{\nu}{\nu_c} \right)^{-p/2} F_{\nu,\max} & \nu_c < \nu. \end{cases} \quad (15)$$

(3) $\nu_m < \nu_c < \nu_a$:

$$F_\nu = F_{\nu,\max} \begin{cases} \left(\frac{\nu}{\nu_m} \right)^2 \left(\frac{\nu_m}{\nu_a} \right)^{(p+4)/2} \left(\frac{\nu_a}{\nu_c} \right)^{-1/2} & \nu < \nu_m, \\ \left(\frac{\nu}{\nu_a} \right)^{5/2} \left(\frac{\nu_a}{\nu_c} \right)^{-p/2} \left(\frac{\nu_c}{\nu_m} \right)^{-(p-1)/2} & \nu_m < \nu < \nu_a, \\ \left(\frac{\nu}{\nu_c} \right)^{-p/2} \left(\frac{\nu_c}{\nu_m} \right)^{-(p-1)/2} & \nu_a < \nu. \end{cases} \quad (16)$$

where $F_{\nu, \max}$ stands for the peak flux density of the spectrum, which can be estimated as

$$F_{\nu, \max} = \frac{N_e P_{\nu, \max}}{4\pi D_L^2}, \quad (17)$$

where N_e is the total number of swept-up electrons in the post-shock fluid. Assuming a spherical geometry, $N_e = 4\pi n(R)R^3/(3-k)$. D_L is the Luminosity distance from the source to the observer. And in the fast cooling regime ($\nu_c < \nu_m$), the self absorption frequency ν_a is:

$$\nu_a = \begin{cases} \left[\frac{c_1 q_e n R}{(3-k) B \gamma_c^5} \right]^{3/5} \nu_c & \nu_a < \nu_c, \\ \left[\frac{c_2 q_e n R}{(3-k) B \gamma_c^5} \right]^{1/3} \nu_c & \nu_c < \nu_a < \nu_m, \\ \left[\frac{c_2 q_e n R}{(3-k) B \gamma_c^5} \right]^{2/(p+5)} \left(\frac{\nu_m}{\nu_c} \right)^{(p-1)/(p+5)} \nu_c & \nu_m < \nu_a. \end{cases} \quad (18)$$

And the flux in fast cooling regime is

(1) $\nu_a < \nu_c < \nu_m$:

$$F_\nu = F_{\nu, \max} \begin{cases} \left(\frac{\nu}{\nu_a} \right)^2 \left(\frac{\nu_a}{\nu_c} \right)^{1/3} & \nu < \nu_a, \\ \left(\frac{\nu}{\nu_c} \right)^{1/3} & \nu_a < \nu < \nu_c, \\ \left(\frac{\nu}{\nu_c} \right)^{-1/2} & \nu_c < \nu < \nu_m, \\ \left(\frac{\nu_m}{\nu_c} \right)^{-1/2} \left(\frac{\nu}{\nu_m} \right)^{-p/2} & \nu_m < \nu. \end{cases} \quad (19)$$

(2) $\nu_c < \nu_a < \nu_m$:

$$F_\nu = F_{\nu, \max} \begin{cases} \left(\frac{\nu}{\nu_c} \right)^2 \left(\frac{\nu_a}{\nu_c} \right)^3 & \nu < \nu_c, \\ \left(\frac{\nu}{\nu_a} \right)^{5/2} \left(\frac{\nu_a}{\nu_c} \right)^{-1/2} & \nu_c < \nu < \nu_a, \\ \left(\frac{\nu}{\nu_c} \right)^{-1/2} & \nu_a < \nu < \nu_m, \\ \left(\frac{\nu_m}{\nu_c} \right)^{-1/2} \left(\frac{\nu}{\nu_m} \right)^{-p/2} & \nu_m < \nu. \end{cases} \quad (20)$$

(3) $\nu_c < \nu_m < \nu_a$:

$$F_\nu = F_{\nu, \max} \begin{cases} \left(\frac{\nu}{\nu_c} \right)^2 \left(\frac{\nu_c}{\nu_a} \right)^3 \left(\frac{\nu_a}{\nu_m} \right)^{-(p-1)/2} & \nu < \nu_c, \\ \left(\frac{\nu}{\nu_a} \right)^{5/2} \left(\frac{\nu_a}{\nu_m} \right)^{-p/2} \left(\frac{\nu_m}{\nu_c} \right)^{-1/2} & \nu_c < \nu < \nu_a, \\ \left(\frac{\nu}{\nu_m} \right)^{-p/2} \left(\frac{\nu_m}{\nu_c} \right)^{-1/2} & \nu_a < \nu. \end{cases} \quad (21)$$

For the point sources outside the LOS, the observed flux needs to be corrected by (Granot et al. 2002)

$$F_\nu = a^3 F_{\nu/a}(at), \quad (22)$$

with a factor

$$a = \frac{1 - \beta}{1 - \beta \cos \theta_{\text{obs}, a}} \approx \frac{1}{1 + \gamma^2 \theta_{\text{obs}, a}^2}, \quad (23)$$

where $\theta_{\text{obs}, a}$ is the angle between LOS and the point source. All point sources with equal $\theta_{\text{obs}, a}$ form a loop around the LOS. We referred to the calculation method of radiation flux proposed by Ghisellini & Lazzati (1999), and the radiation flux of the entire jet is obtained by integrating over $\theta_{\text{obs}, a}$. But only the portion of each loop within the jet contributes to the total radiation (see Figure 1). Assuming that the proportion of the corresponding ring at $\theta_{\text{obs}, a}$ within the i -th component is $\chi_i(\theta_{\text{obs}, a})/2\pi$. Overall, the total radiation flux can be calculated as

$$F_\nu(t) = \sum_{i=1}^n \int_0^\infty a^3 F_{\nu/a, i}(at) \frac{\chi_i(\theta_{\text{obs}, a})}{2\pi} d\theta_{\text{obs}, a}. \quad (24)$$

Table 1. The fitting parameters. The best-fit values are the maximum likelihood parameters from the posterior distribution of the MCMC sample. For comparison, we also present the initial settings of the MCMC and the medians of the posterior distribution with the 1σ range of the MCMC samples.

		parameters	best fit	initial	posterior
Components' parameters	Lorentz factors	$\gamma_{0,1}$	203.7	316.2	$178.2^{+106.9}_{-42.7}$
		$\gamma_{0,2}$	610.9	199.5	$364.8^{+302.0}_{-181.1}$
		$\gamma_{0,3}$	373.2	505.8	$516.4^{+336.7}_{-290.5}$
	Isotropic kinetic energy (erg)	$E_{k,iso,1}$	5.0×10^{52}	1.6×10^{52}	$3.3^{+2.8}_{-1.4} \times 10^{52}$
		$E_{k,iso,2}$	1.0×10^{55}	2.1×10^{54}	$4.9^{+3.7}_{-2.8} \times 10^{54}$
		$E_{k,iso,3}$	1.6×10^{54}	4.0×10^{53}	$8.2^{+5.7}_{-3.6} \times 10^{53}$
	Polar angles of axes	θ_1	0.004	0.011	$0.003^{+0.010}_{-0.002}$
		θ_2	0.038	0.051	$0.046^{+0.009}_{-0.005}$
		θ_3	0.028	0.035	$0.036^{+0.008}_{-0.006}$
	Azimuth angles of axes	φ_1	1.9	1.0	$1.1^{+0.6}_{-0.7}$
		φ_2	3.4	3.2	$3.0^{+0.6}_{-0.6}$
		φ_3	5.2	4.9	$5.0^{+0.8}_{-0.7}$
	Half-opening angles	$\theta_{r,1}$	0.020	0.023	$0.018^{+0.008}_{-0.004}$
		$\theta_{r,2}$	0.011	0.019	$0.015^{+0.008}_{-0.005}$
		$\theta_{r,3}$	0.012	0.014	$0.016^{+0.008}_{-0.005}$
Other parameters	Shock energy into electrons	ϵ_e	0.24	0.29	$0.27^{+0.07}_{-0.05}$
	Shock energy into magnetic field	ϵ_B	5.1×10^{-5}	1.6×10^{-4}	$9.5^{+1.1}_{-7.1} \times 10^{-5}$
	Particle number density (cm^{-3})	n	0.42	1.0	$0.82^{+0.54}_{-0.29}$
	Distribution index of electrons	p	2.8	2.8	$2.8^{+0.03}_{-0.03}$
	View angle	θ_{obs}	7.4×10^{-4}	3.9×10^{-4}	$3.8^{+18.1}_{-3.4} \times 10^{-4}$
	View azimuth	φ_{obs}	2.6	2.4	$2.8^{+2.0}_{-1.9}$
	underestimated fraction of variance	f	0.036	1.0	$0.040^{+0.005}_{-0.004}$

3.1. Fitting results

In this work, we used an asymmetric jet with 3 components to analyze multi-band observation data from multiple telescopes (de Wet et al. 2023). And the MCMC method was used to fit the multi-band data of GRB 210731A. We assume that the jet decelerates in uniform interstellar medium ($k = 0$, the particle density n is a constant).

The emcee (Foreman-Mackey et al. 2013) was applied to the MCMC analysis of the observation data of GRB 210731A. We used 44 walkers and 32312 steps, and found a set of parameters to fit the multi-band observation data. Our results indicate that the 3-component asymmetric jet model fits the multi-band light curve of GRB 210731A well ¹. The best-fit values of these parameters are summarized in Table 1. As a comparison, the initial values and posterior distributions obtained from MCMC are also presented in it. Figure 2 shows the MCMC fitting results for all parameters. The best-fit values of these parameters and the $1 - \sigma$ ranges of their posterior distributions are marked in Figure 2 with red solid lines and black dashed lines, respectively. The best fitting results of the light curves with respect to the multi-band afterglow data are shown as solid lines in Figure 3. To better illustrate the fitting details, we separately display the fitting results for X-ray, q-band, and X-band in Figure 4, as well as the radiation contributions of the three components. Additionally, the $1 - \sigma$ range of the light curves corresponding to the MCMC samples is depicted as pink shaded regions near the light curves of the total radiation flux. To quantitatively express the goodness of the fit, we applied the adjusted coefficient of determination, R^2_{adj} , to analyze the light curve corresponding to the best-fit values of these parameters ². Moreover, we obtained $R^2_{adj} \sim 0.91$, which is close enough to 1 to indicate that our model fits the data well.

¹ In the uvw1, uvm2, and uvw2 bands, the theoretical light curves are slightly higher than the observed data, which should be due to the uncertainty of extinction of ultraviolet bump in the host galaxy (Corre et al. 2018). As for the data in the r-band and g-band after 10^7 s, it is consistent with the radiation of the host galaxy (de Wet et al. 2023).

² The coefficient of determination, R^2 , quantifies how well the model explains the data by comparing the residual sum of squares, SS_{res} , to the total sum of squares, SS_{tot} , of the observed data. It is defined as $R^2 = 1 - SS_{res}/SS_{tot}$, where SS_{tot} represents the sum of the squared deviations of the observed values from their mean, reflecting the inherent variability in the data. An R^2 value closer to 1 indicates that more variability is explained by the model, demonstrating a better fit. To avoid inflated R^2 in models with many parameters, we use the adjusted coefficient of determination, $R^2_{adj} = 1 - (1 - R^2)(N - 1)/(N - P - 1)$, where N is the number of data points and P is the number of parameters.

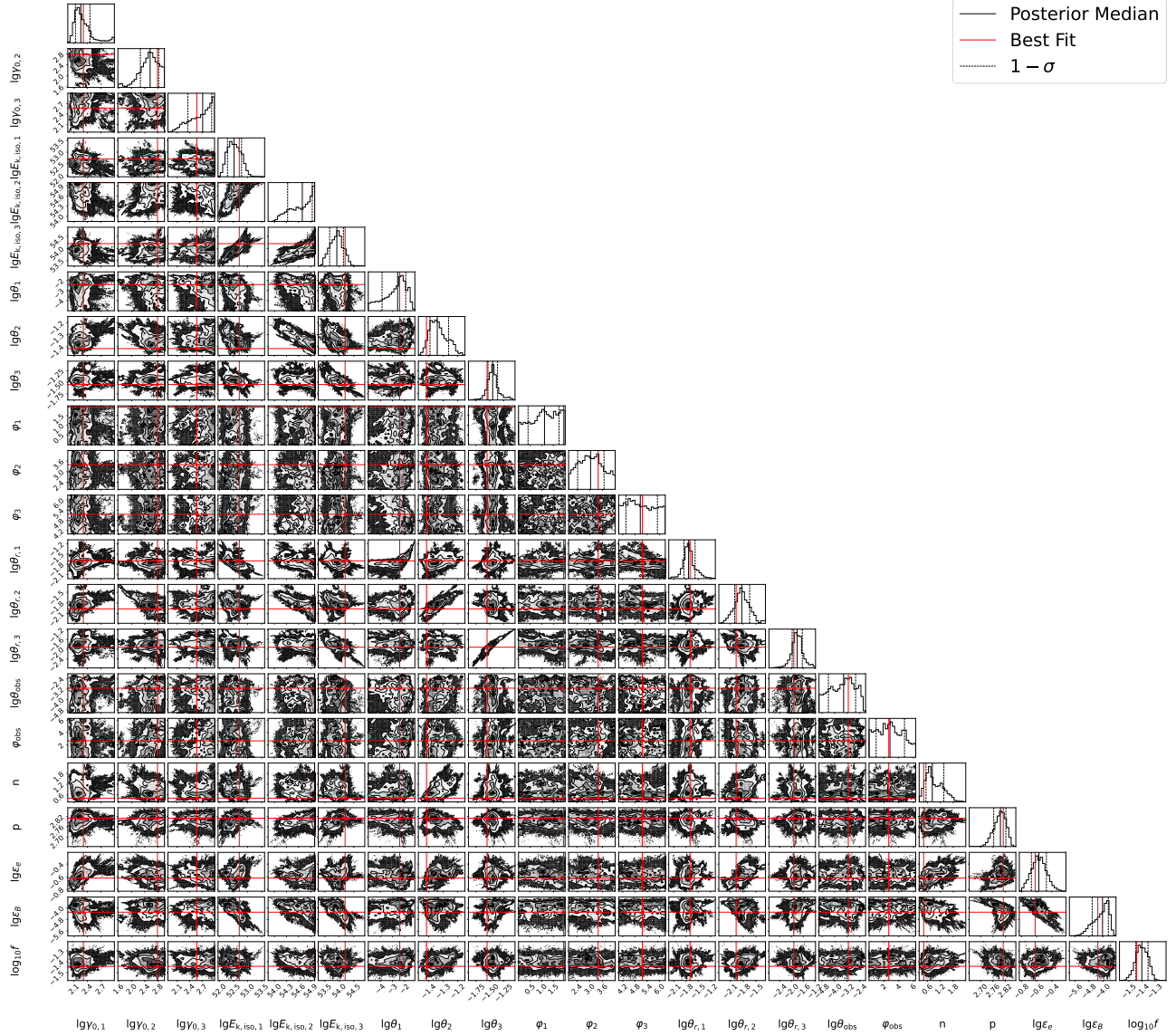


Figure 2. The fitting results of MCMC on all parameters. The best-fit values are marked with red crosses and solid red lines. The solid black lines represent the median values of the posterior distributions of the parameters. The range of $1 - \sigma$ for each parameter’s posterior distribution is located between two dashed lines. The fraction f , which underestimates the variance of the data, is used as a free parameter for fitting.

Our results indicate that the afterglow generated by the deceleration of three independent components of a jet in the uniform interstellar medium provides a good fit to the multi-band observation data. Among these three components, a higher velocity is associated with higher energy. The fastest component has a Lorentz factor exceeding 600, with an equivalent isotropic kinetic energy approaching 10^{55} ergs. In contrast, the slowest component has a Lorentz factor of around 200, with an equivalent isotropic kinetic energy of 1.6×10^{52} ergs. The difference in Lorentz factors exceeds 400, and their equivalent isotropic kinetic energies differ by approximately 2.3 orders of magnitude. Given this context, the presence of a medium-speed component, characterized by a Lorentz factor of about 370, is notable. This component is much closer to the slowest component in terms of velocity (by approximately 170), while its energy lies between that of the other two components. Furthermore, the schematic diagram of the relative positions and sizes of the cross-sections of the three components based on the best-fit parameter values is shown in Figure 1. The projection of LOS on the components’ cross-sections is marked with a black point. We found that the LOS is localized in the component with the lowest energy and slowest speed. And the observer’s LOS almost coincides with the axis of the component. As

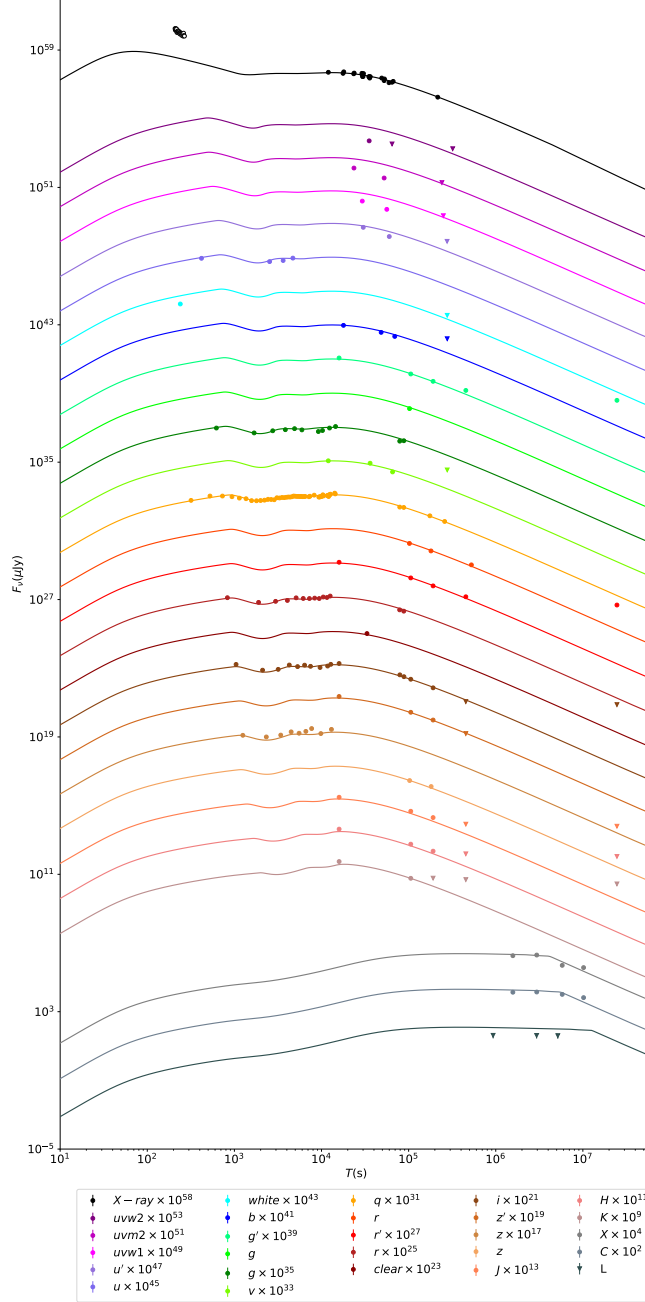


Figure 3. Multi-band afterglow data of GRB 210731A and the best fitting result. The observation data of each band is represented by points, with the inverted triangle representing the upper limit. And the hollow dots of X-ray at early time are considered as high latitude prompt emission. The theoretical light curves corresponds to the solid line.

a result, the component with the lowest energy and slowest speed was observed earliest, dominating the first peak in the light curve of the optical afterglow. Among the remaining two components, the component with medium energy and speed is closer to the LOS, thus contributing to the second peak in the light curve of the optical afterglow. In contrast, the component with the highest energy and speed forms the largest angle with the LOS among the three components, causing its afterglow to be observed last and producing the final and brightest peak in the light curve of the optical afterglow. At the same time, the late-stage radiation in the X-ray and radio bands from the component with the highest energy and speed can also be well fitted to the observed data.

4. CONCLUSIONS AND DISCUSSION

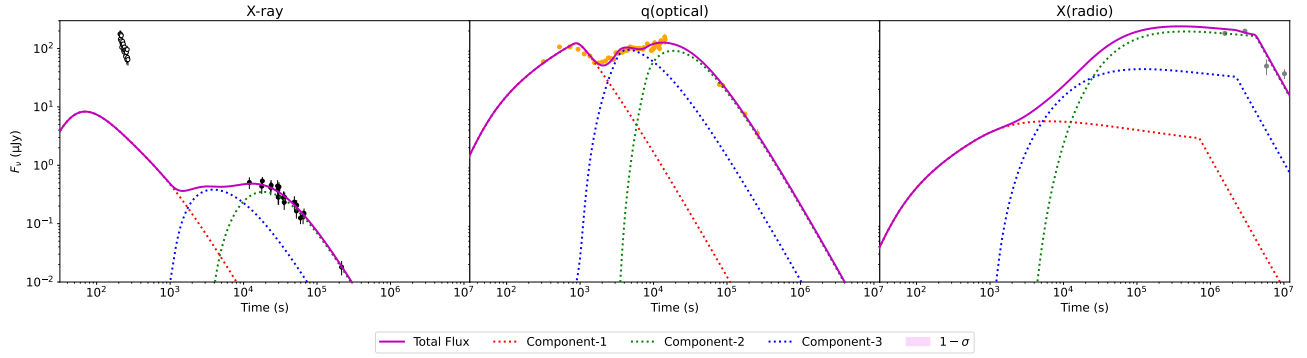


Figure 4. Same as Figure 3, but we have shown the details of the X-ray, q-band, and X-band light curves. The solid line is the total flux of the jet. The $1 - \sigma$ range of total radiation flux has been marked with pink shadow. And the dashed lines of different colors respectively represent the radiation of three components. The triple peaks exhibited in the optical band correspond to the radiation peaks of the three components.

In recent years, observations of several famous GRBs, such as the one associated with gravitational waves (GRB 170817A; Abbott et al. 2017; Kasliwal et al. 2017; Xiao et al. 2017; Gao 2018; Gottlieb et al. 2018; Lazzati et al. 2018; Lyman et al. 2018; Piro & Kollmeier 2018; Troja et al. 2018; Zhang et al. 2018) and the one known as the “brightest of all time” (GRB 221009A; An et al. 2023; O’Connor et al. 2023), have suggested that GRB jets may be structured. The interpretations of the radio rebrightening in tidal disruption events Sw J1644+57 and AT2022cmc, support that these events may contain a structured jet (Wang et al. 2014; Zhou et al. 2024). Another interesting GRB source that was recently detected, GRB 210731A, displayed multiple rebrightening features in its optical afterglow. Through MCMC fitting, we show that a multi-component asymmetric structured jet can well explain the multi-band afterglow data of GRB 210731A.

Theoretically, there could be several potential causes for this multi-component asymmetric structured jets. For example, the presence of significant non-uniformity in the internal magnetic dissipation of a jet can lead to the development of complex and asymmetric jet structures (Narayan & Kumar 2009). A more recent study conducted by Huang et al. (2019) has demonstrated that the non-uniformity of jets can exist in the circumferential direction due to the precession of GRBs’ central engine. Lamb et al. (2022) used the results of the three-dimensional hydrodynamic jets in the neutron star merger environment to determine the degree of polar and rotational inhomogeneity ($N \times N$ jet model). They found that the result of these inhomogeneities in the jet’s energy/Lorentz factor distribution showed some degree of rotational variation.

Distinct from the energy injection model in the stellar wind environment employed by de Wet et al. (2023), we found that the multi-band observation data of the afterglow of GRB 210731A can be well fitted by the deceleration of three independent components of a jet in the uniform interstellar medium. It is noteworthy that, both in the stellar wind environment of de Wet et al. (2023) and in our uniform interstellar medium, the theoretical light curves exceed the upper limit of the L-band. Furthermore, corresponding to our best-fit parameters, the self-absorption frequency of the highest-energy component lies between approximately 1.7×10^9 Hz and 1.9×10^9 Hz around 10^6 to 10^7 seconds, which is slightly higher than the L-band. This contrasts with de Wet et al. (2023)’s conclusion that in a stellar wind environment, the self-absorption frequency is almost impossible to occur between the L-band and C-band. Therefore, we believe that the additional sources of opacity are required to constrain the upper limit of the L-band, similar to de Wet et al. (2023)’s inference, which suggests an abundance of thermal electrons in the shock region.

Compared to the energy injection model, the structured jet model does not place stringent requirements on the central engine and circumstellar environment when explaining the data of GRB 210731A. However, it is important to emphasize that the ability to distinguish between the two models is very limited based solely on the fitting of light curves, even with multi-band data fitting. To truly distinguish between these two models for similar gamma-ray bursts in the future, polarimetric observations are important. The energy injection model does not, in principle, significantly affect the polarization properties of the afterglow, while under the structured jet model, the afterglow signal will exhibit significant polarization features (Lazzati et al. 2003; Rossi et al. 2004; Nakar & Oren 2004; Wu et al. 2005), especially when the jet structure is non-axisymmetric, resulting in a significant evolution of the polarization angle (Li et al. 2024). Future polarimetric observations of GRB afterglows will play a crucial role in revealing the jet structure.

ACKNOWLEDGEMENTS

This work is supported by the National Natural Science Foundation of China (Projects 12373040,12021003,12473012) and the Fundamental Research Funds for the Central Universities and the Carlsberg Foundation (CF18-0183, PI: I. Tamborra).

REFERENCES

- Abbott, B. P., Abbott, R., Abbott, T. D., et al. 2017, *Phys. Rev. Lett.*, 119, 161101, doi: [10.1103/PhysRevLett.119.161101](https://doi.org/10.1103/PhysRevLett.119.161101)
- An, Z.-H., Antier, S., Bi, X.-Z., et al. 2023, arXiv e-prints, arXiv:2303.01203, doi: [10.48550/arXiv.2303.01203](https://doi.org/10.48550/arXiv.2303.01203)
- Barthelmy, S. D., Barbier, L. M., Cummings, J. R., et al. 2005, *SSRv*, 120, 143, doi: [10.1007/s11214-005-5096-3](https://doi.org/10.1007/s11214-005-5096-3)
- Beniamini, P., Granot, J., & Gill, R. 2020, *MNRAS*, 493, 3521, doi: [10.1093/mnras/staa538](https://doi.org/10.1093/mnras/staa538)
- Bloemen, S., Groot, P., Woudt, P., et al. 2016, in *Society of Photo-Optical Instrumentation Engineers (SPIE) Conference Series*, Vol. 9906, *Ground-based and Airborne Telescopes VI*, ed. H. J. Hall, R. Gilmozzi, & H. K. Marshall, 990664, doi: [10.1117/12.2232522](https://doi.org/10.1117/12.2232522)
- Burrows, D. N., Hill, J. E., Nousek, J. A., et al. 2005, *SSRv*, 120, 165, doi: [10.1007/s11214-005-5097-2](https://doi.org/10.1007/s11214-005-5097-2)
- Corre, D., Buat, V., Basa, S., et al. 2018, *A&A*, 617, A141, doi: [10.1051/0004-6361/201832926](https://doi.org/10.1051/0004-6361/201832926)
- Costa, E., Frontera, F., Heise, J., et al. 1997, *Nature*, 387, 783, doi: [10.1038/42885](https://doi.org/10.1038/42885)
- Dai, Z. G., & Lu, T. 1998, *A&A*, 333, L87, doi: [10.48550/arXiv.astro-ph/9810402](https://doi.org/10.48550/arXiv.astro-ph/9810402)
- . 1999, *ApJL*, 519, L155, doi: [10.1086/312127](https://doi.org/10.1086/312127)
- de Wet, S., Laskar, T., Groot, P. J., et al. 2023, *A&A*, 671, A116, doi: [10.1051/0004-6361/202244917](https://doi.org/10.1051/0004-6361/202244917)
- Filippenko, A. V., Li, W. D., Treffers, R. R., & Modjaz, M. 2001, in *Astronomical Society of the Pacific Conference Series*, Vol. 246, *IAU Colloq. 183: Small Telescope Astronomy on Global Scales*, ed. B. Paczynski, W.-P. Chen, & C. Lemme, 121
- Foreman-Mackey, D., Hogg, D. W., Lang, D., & Goodman, J. 2013, *PASP*, 125, 306, doi: [10.1086/670067](https://doi.org/10.1086/670067)
- Frail, D. A., Kulkarni, S. R., Nicastro, L., Feroci, M., & Taylor, G. B. 1997, *Nature*, 389, 261, doi: [10.1038/38451](https://doi.org/10.1038/38451)
- Gao, H. 2018, *Science China Physics, Mechanics, and Astronomy*, 61, 59531, doi: [10.1007/s11433-017-9149-3](https://doi.org/10.1007/s11433-017-9149-3)
- Gao, H., Lei, W.-H., Zou, Y.-C., Wu, X.-F., & Zhang, B. 2013, *NewAR*, 57, 141, doi: [10.1016/j.newar.2013.10.001](https://doi.org/10.1016/j.newar.2013.10.001)
- Gehrels, N., Chincarini, G., Giommi, P., et al. 2004, *ApJ*, 611, 1005, doi: [10.1086/422091](https://doi.org/10.1086/422091)
- Ghisellini, G., & Lazzati, D. 1999, *MNRAS*, 309, L7, doi: [10.1046/j.1365-8711.1999.03025.x](https://doi.org/10.1046/j.1365-8711.1999.03025.x)
- Gill, R., & Granot, J. 2023, *MNRAS*, doi: [10.1093/mnras/stad3991](https://doi.org/10.1093/mnras/stad3991)
- Gottlieb, O., Nakar, E., & Bromberg, O. 2021, *MNRAS*, 500, 3511, doi: [10.1093/mnras/staa3501](https://doi.org/10.1093/mnras/staa3501)
- Gottlieb, O., Nakar, E., Piran, T., & Hotokezaka, K. 2018, *MNRAS*, 479, 588, doi: [10.1093/mnras/sty1462](https://doi.org/10.1093/mnras/sty1462)
- Granot, J., Panaitescu, A., Kumar, P., & Woosley, S. E. 2002, *ApJL*, 570, L61, doi: [10.1086/340991](https://doi.org/10.1086/340991)
- Greiner, J., Bornemann, W., Clemens, C., et al. 2008, *PASP*, 120, 405, doi: [10.1086/587032](https://doi.org/10.1086/587032)
- Greiner, J., Krühler, T., McBreen, S., et al. 2009, *ApJ*, 693, 1912, doi: [10.1088/0004-637X/693/2/1912](https://doi.org/10.1088/0004-637X/693/2/1912)
- Huang, B.-Q., Lin, D.-B., Liu, T., et al. 2019, *MNRAS*, 487, 3214, doi: [10.1093/mnras/stz1426](https://doi.org/10.1093/mnras/stz1426)
- Huang, Y.-f., Dai, Z.-g., & Lu, T. 1999a, *Chinese Physics Letters*, 16, 775, doi: [10.1088/0256-307X/16/10/027](https://doi.org/10.1088/0256-307X/16/10/027)
- Huang, Y. F., Dai, Z. G., & Lu, T. 1999b, *MNRAS*, 309, 513, doi: [10.1046/j.1365-8711.1999.02887.x](https://doi.org/10.1046/j.1365-8711.1999.02887.x)
- Huang, Y. F., Gou, L. J., Dai, Z. G., & Lu, T. 2000, *ApJ*, 543, 90, doi: [10.1086/317076](https://doi.org/10.1086/317076)
- Huang, Y. F., Wu, X. F., Dai, Z. G., Ma, H. T., & Lu, T. 2004, *ApJ*, 605, 300, doi: [10.1086/382202](https://doi.org/10.1086/382202)
- Kann, D. A., Izzo, L., Levan, A. J., et al. 2021, *GRB Coordinates Network*, 30583, 1
- Kasliwal, M. M., Nakar, E., Singer, L. P., et al. 2017, *Science*, 358, 1559, doi: [10.1126/science.aap9455](https://doi.org/10.1126/science.aap9455)
- Kuin, N. P. M., Troja, E., & Swift/UVOT Team. 2021, *GRB Coordinates Network*, 30572, 1
- Lamb, G. P., Nativi, L., Rosswog, S., et al. 2022, *Universe*, 8, 612, doi: [10.3390/universe8120612](https://doi.org/10.3390/universe8120612)
- Lazzati, D., Perna, R., Morsony, B. J., et al. 2018, *PhRvL*, 120, 241103, doi: [10.1103/PhysRevLett.120.241103](https://doi.org/10.1103/PhysRevLett.120.241103)
- Lazzati, D., Covino, S., di Serego Alighieri, S., et al. 2003, *A&A*, 410, 823, doi: [10.1051/0004-6361:20031321](https://doi.org/10.1051/0004-6361:20031321)
- Li, J.-D., Gao, H., Ai, S., & Lei, W.-H. 2023, *Monthly Notices of the Royal Astronomical Society*, stad2606, doi: [10.1093/mnras/stad2606](https://doi.org/10.1093/mnras/stad2606)
- . 2024, submitted
- Lyman, J. D., Lamb, G. P., Levan, A. J., et al. 2018, *Nature Astronomy*, 2, 751, doi: [10.1038/s41550-018-0511-3](https://doi.org/10.1038/s41550-018-0511-3)
- Mangano, V., Holland, S. T., Malesani, D., et al. 2007, *A&A*, 470, 105, doi: [10.1051/0004-6361:20077232](https://doi.org/10.1051/0004-6361:20077232)

- Mészáros, P., & Rees, M. J. 1997, *ApJ*, 476, 232, doi: [10.1086/303625](https://doi.org/10.1086/303625)
- Nakar, E., & Oren, Y. 2004, *ApJL*, 602, L97, doi: [10.1086/382729](https://doi.org/10.1086/382729)
- Narayan, R., & Kumar, P. 2009, *MNRAS*, 394, L117, doi: [10.1111/j.1745-3933.2009.00624.x](https://doi.org/10.1111/j.1745-3933.2009.00624.x)
- Nicuesa Guelbenzu, A., Klose, S., Schmidl, S., & Rau, A. 2021a, *GRB Coordinates Network*, 30574, 1
- Nicuesa Guelbenzu, A., Klose, S., Schmidl, S., Rau, A., & Kann, D. A. 2021b, *GRB Coordinates Network*, 30584, 1
- O'Connor, B., Troja, E., Ryan, G., et al. 2023, *Science Advances*, 9, eadi1405, doi: [10.1126/sciadv.adi1405](https://doi.org/10.1126/sciadv.adi1405)
- Peng, F., Königl, A., & Granot, J. 2005, *ApJ*, 626, 966, doi: [10.1086/430045](https://doi.org/10.1086/430045)
- Perley, R. A., Chandler, C. J., Butler, B. J., & Wrobel, J. M. 2011, *ApJL*, 739, L1, doi: [10.1088/2041-8205/739/1/L1](https://doi.org/10.1088/2041-8205/739/1/L1)
- Piro, A. L., & Kollmeier, J. A. 2018, *ApJ*, 855, 103, doi: [10.3847/1538-4357/aaaab3](https://doi.org/10.3847/1538-4357/aaaab3)
- Roming, P. W. A., Kennedy, T. E., Mason, K. O., et al. 2005, *SSRv*, 120, 95, doi: [10.1007/s11214-005-5095-4](https://doi.org/10.1007/s11214-005-5095-4)
- Rossi, E. M., Lazzati, D., Salmonson, J. D., & Ghisellini, G. 2004, *MNRAS*, 354, 86, doi: [10.1111/j.1365-2966.2004.08165.x](https://doi.org/10.1111/j.1365-2966.2004.08165.x)
- Sari, R., Piran, T., & Narayan, R. 1998, *ApJL*, 497, L17, doi: [10.1086/311269](https://doi.org/10.1086/311269)
- Stamatikos, M., Barthelmy, S. D., Krimm, H. A., et al. 2021, *GRB Coordinates Network*, 30580, 1
- Swenson, C. A., Roming, P. W. A., De Pasquale, M., & Oates, S. R. 2013, *ApJ*, 774, 2, doi: [10.1088/0004-637X/774/1/2](https://doi.org/10.1088/0004-637X/774/1/2)
- Troja, E., Ambrosi, E., D'Elia, V., et al. 2021, *GRB Coordinates Network*, 30568, 1
- Troja, E., Piro, L., Ryan, G., et al. 2018, *MNRAS*, 478, L18, doi: [10.1093/mnrasl/sly061](https://doi.org/10.1093/mnrasl/sly061)
- van Paradijs, J., Groot, P. J., Galama, T., et al. 1997, *Nature*, 386, 686, doi: [10.1038/386686a0](https://doi.org/10.1038/386686a0)
- Wang, J.-Z., Lei, W.-H., Wang, D.-X., et al. 2014, *ApJ*, 788, 32, doi: [10.1088/0004-637X/788/1/32](https://doi.org/10.1088/0004-637X/788/1/32)
- Wang, X.-G., Zhang, B., Liang, E.-W., et al. 2015, *ApJS*, 219, 9, doi: [10.1088/0067-0049/219/1/9](https://doi.org/10.1088/0067-0049/219/1/9)
- Wu, X. F., Dai, Z. G., Huang, Y. F., & Lu, T. 2003, *MNRAS*, 342, 1131, doi: [10.1046/j.1365-8711.2003.06602.x](https://doi.org/10.1046/j.1365-8711.2003.06602.x)
- . 2005, *MNRAS*, 357, 1197, doi: [10.1111/j.1365-2966.2005.08685.x](https://doi.org/10.1111/j.1365-2966.2005.08685.x)
- Xiao, D., Liu, L.-D., Dai, Z.-G., & Wu, X.-F. 2017, *ApJL*, 850, L41, doi: [10.3847/2041-8213/aa9b2b](https://doi.org/10.3847/2041-8213/aa9b2b)
- Zhang, B., Fan, Y. Z., Dyks, J., et al. 2006, *ApJ*, 642, 354, doi: [10.1086/500723](https://doi.org/10.1086/500723)
- Zhang, B. B., Zhang, B., Sun, H., et al. 2018, *Nature Communications*, 9, 447, doi: [10.1038/s41467-018-02847-3](https://doi.org/10.1038/s41467-018-02847-3)
- Zheng, W., Filippenko, A. V., & KAIT GRB Team. 2021, *GRB Coordinates Network*, 30582, 1
- Zhou, C., Zhu, Z.-P., Lei, W.-H., et al. 2024, *ApJ*, 963, 66, doi: [10.3847/1538-4357/ad20f3](https://doi.org/10.3847/1538-4357/ad20f3)